Supplementary Information to "The influence of layering and barometric pumping on firn air transport in a 2D model"

Benjamin Birner[1], Christo Buizert[2], Till J.W. Wagner[1] and Jeffrey P. Severinghaus[1]

[1]Scripps Institution of Oceanography, University of California San Diego, La Jolla, CA 92093, USA
5   [2]College of Earth, Ocean and Atmospheric Sciences, Oregon State University, Corvallis, OR 97331, USA

Correspondence to: Benjamin Birner (bbirner@ucsd.edu)

1   2D trace gas transport model

1.1   Numerical integration scheme

Trace gas migration in firn is governed by the partial differential Eq. (S1):

$$\tilde{s}\frac{\partial q}{\partial t} = \vec{\nabla} \cdot \left[\tilde{s}\boldsymbol{D}_m\left(\vec{\nabla}q - \vec{G}\,q + \Omega\frac{\partial T}{\partial z}q\,\hat{k}\right)\right] + \vec{\nabla}\cdot\left[\tilde{s}\boldsymbol{D}_d\vec{\nabla}q\right] - (\tilde{s}\,\vec{u})\cdot\vec{\nabla}q\,, \tag{S1}$$

10   where $\vec{G} \equiv \frac{\Delta m\,\bar{g}}{R\,T}$, $q \equiv \frac{\delta}{1000} + 1$ is the trace gas or isotope mixing ratio, $\tilde{s} \equiv s_{op}\exp\left(\frac{M\,g}{R\,T}z\right)$ pressure-corrected open porosity ($m^3\,m^{-3}$), T temperature (K), Δm isotope mass difference (kg mol^{-1}) to the mass of air M (kg mol^{-1}), $\bar{g}$ gravitational acceleration (m s^{-2}), R the fundamental gas constant (J mol^{-1} K^{-1}), $\vec{u}$ air advection velocity due to snow accumulation, pore compression and barometric pumping (m s^{-1}), and Ω thermal diffusion sensitivity (K^{-1}). $\boldsymbol{D}_m$ is the molecular diffusivity and $\boldsymbol{D}_d$ is the dispersion tensor (m^2 s^{-1}). $\boldsymbol{D}_m$ has different entries on the diagonal to represent different strengths of molecular diffusion in
15   the vertical and horizontal direction. Similarly, $\boldsymbol{D}_d$ is simplified to an "eddy diffusivity", $\boldsymbol{D}_e$, acting in vertical and horizontal direction as described in the text. $\tilde{s} = \tilde{s}(z)$, $T = \text{T}(z,t)$, and $q = q(x,z,t)$ are scalar fields. Furthermore, $\vec{u} = u(x,z,t)\,\hat{\imath} + w(x,z,t)\,\hat{k}$ is a vector field and $\vec{\nabla} \equiv \frac{\partial}{\partial x}\hat{\imath} + \frac{\partial}{\partial z}\hat{k}$ is the gradient operator.

Equation (S1) is discretized using a Crank-Nicolson time stepping scheme and central difference approximations derived from flux balance on an Arakawa C (i.e., staggered; Fig. S1) grid as follows:

$$\tilde{s}(z)\frac{q(x,z,t+\Delta t) - q(x,z,t)}{\Delta t} = \frac{1}{2}\left[(\mathbf{A}+\mathbf{B})_{|t+\Delta t}\,q(x,z,t+\Delta t) + (\mathbf{A}+\mathbf{B})_{|t}\,q(x,z,t)\right], \tag{S2}$$

20   where

$$\mathbf{A}_{|t}\,q(x,z,t) \equiv \frac{-\tilde{s}u\left(x+\frac{\Delta x}{2},z,t\right)}{2\Delta x}q(x+\Delta x,z,t) + \frac{\tilde{s}u\left(x-\frac{\Delta x}{2},z,t\right)}{2\Delta x}q(x-\Delta x,z,t) - \frac{\tilde{s}w\left(x,z+\frac{\Delta z}{2},t\right)}{2\Delta z}q(x,z+\Delta z,t) +$$

$$\frac{\tilde{s}w\left(x,z-\frac{\Delta z}{2},t\right)}{2\Delta z}q(x,z-\Delta z,t) + \left[\frac{\tilde{s}u\left(x+\frac{\Delta x}{2},z,t\right)-\tilde{s}u\left(x-\frac{\Delta x}{2},z,t\right)}{2\Delta x} + \frac{\tilde{s}w\left(x,z+\frac{\Delta z}{2},t\right)-\tilde{s}w\left(x,z-\frac{\Delta z}{2},t\right)}{2\Delta z}\right]q(x,z,t)\,, \tag{S3}$$

$$\mathbf{B}_{|t}\, q(x,z,t) \equiv \frac{\tilde{s}D_h^*\left(x+\frac{\Delta x}{2},z,t\right)}{\Delta x^2}q(x+\Delta x,z,t) + \frac{\tilde{s}D_h^*\left(x-\frac{\Delta x}{2},z,t\right)}{\Delta x^2}q(x-\Delta x,z,t) + \left[\frac{\tilde{s}D_v^*\left(x,z+\frac{\Delta z}{2},t\right)}{\Delta z^2} - G\,\frac{\tilde{s}D_{m,v}\left(x,z+\frac{\Delta z}{2},t\right)}{2\Delta z} + \right.$$

$$\left. \frac{\tilde{s}D_{m,v}\Omega\left(x,z+\frac{\Delta z}{2}\right)\left(\frac{T(x,z+\Delta z,t)-T(x,z,t)}{\Delta z}\right)}{2\Delta z}\right]q(x,z+\Delta z,t) + \left[\frac{\tilde{s}D_v^*\left(x,z-\frac{\Delta z}{2},t\right)}{\Delta z^2} + G\,\frac{\tilde{s}D_{m,v}\left(x,z-\frac{\Delta z}{2},t\right)}{2\Delta z} - \right.$$

$$\left. \frac{\tilde{s}D_{m,v}\Omega\left(x,z-\frac{\Delta z}{2}\right)\left(\frac{T(x,z,t)-T(x,z-\Delta z,t)}{\Delta z}\right)}{2\Delta z}\right]q(x,z-\Delta z,t) + \left[-\frac{\tilde{s}D_h^*\left(x+\frac{\Delta x}{2},z,t\right)+\tilde{s}D_h^*\left(x-\frac{\Delta x}{2},z,t\right)}{\Delta x^2} - \frac{\tilde{s}D_v^*\left(x,z+\frac{\Delta z}{2},t\right)+\tilde{s}D_v^*\left(x,z-\frac{\Delta z}{2},t\right)}{\Delta z^2} + \right.$$

$$\left. G\,\frac{\tilde{s}D_{m,v}\left(x,z-\frac{\Delta z}{2},t\right)-\tilde{s}D_{m,v}\left(x,z+\frac{\Delta z}{2},t\right)}{2\Delta z} + \frac{\tilde{s}D_{m,v}\Omega\left(x,z+\frac{\Delta z}{2}\right)\left(\frac{T(x,z+\Delta z,t)-T(x,z,t)}{\Delta z}\right)-\tilde{s}D_{m,v}\Omega\left(x,z-\frac{\Delta z}{2}\right)\left(\frac{T(x,z,t)-T(x,z-\Delta z,t)}{\Delta z}\right)}{2\Delta z}\right]q(x,z,t)\,, \tag{S4}$$

with $\boldsymbol{D}^* \equiv \boldsymbol{D}_e + \boldsymbol{D}_m$ a combination of eddy and molecular diffusivity in vertical (D_v^*) and horizontal (D_h^*) direction, Δt time step of integration (s), Δz vertical grid spacing (m), and Δx horizontal grid spacing (m). Here q is a Nx1 vectors where N is the number of grid cells; **A** and **B** are banded square-matrices of dimensions NxN that represent the advection operator (i.e., the sum of the three velocity components) and the diffusion operator (Fickian diffusion, eddy diffusion, thermal diffusion, and gravitational fractionation), respectively. The two matrices have entries on the diagonal as well as four off diagonals corresponding to the grid points above, below, to the left and to the right. Because **A** and **B** are also dependent on time, subscripts indicate the time step in Eqs. (S3) and (S4). Equations (S2) – (S4) form a system of linear equations describing the change in time of q at all spatial points. Rearranging Eq. (S2) yields

$$(x,z,t+\Delta t) = \left[\tilde{s}(z)\,\mathbf{I} - (\mathbf{A}+\mathbf{B})_{|t+\Delta t}\right]^{-1}\left[\frac{\Delta t}{2}(\mathbf{A}+\mathbf{B})_{|t} + \tilde{s}(z)\,\mathbf{I}\right]q(x,z,t)\,, \tag{S5}$$

with **I** the identity matrix, which can be stepped forward in time. In the limit of no horizontal transport and constant coefficients ($\tilde{s}$, D_m, D_e and $\vec{u}$ constant), we find good agreement between our numerical model and analytical solutions for a simple 1D model (Appendix A, Fig. S2). δ^{15}N profiles from the model run at 5x higher temporal resolution indicate that the error introduced by a coarser time step converges and is small (~0.5 per meg) relative to the signal in the deep firn (~5 per meg) (Fig. S3).
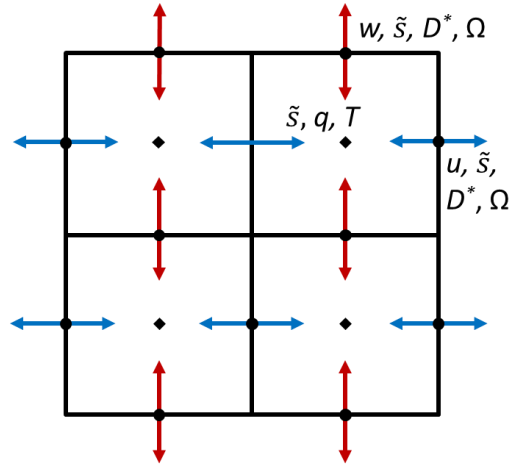
Figure S1. Schematic of the distribution of variables $q, T, u, \tilde{s}, D^*, \Omega$ and w on the staggered grid.
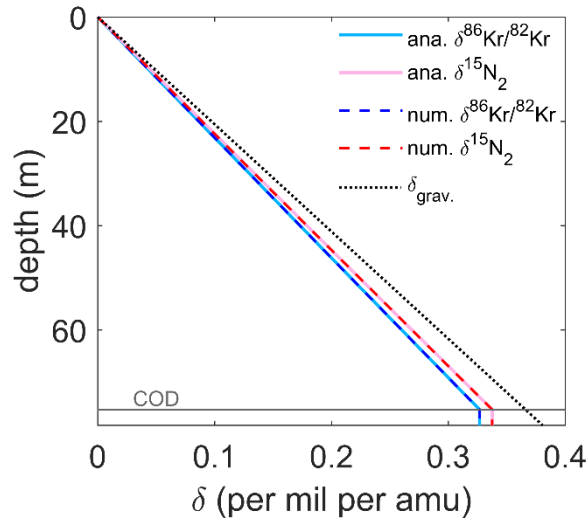
Figure S2. Comparison of 1D analytical solutions (Appendix A, solid lines) and numerical model output (dashed coloured lines). Here $w = 10^{-9}$ m s^{-1}, $D_e = 6 \times 10^{-7}$ m^2 s^{-1} and molecular diffusivity of CO_2 $D_m = 6 \times 10^{-6}$ m^2 s^{-1} up to the COD The dashed black line shows the gravitational settling equilibrium, i.e., the steady-state solution for each isotope pair neglecting advection and non-fractionating mixing processes (δ_{grav}).
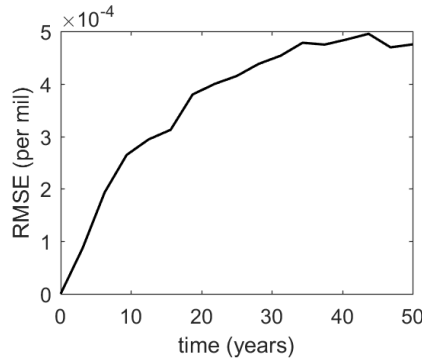
Figure S3. Evolution of the root-mean-square difference between the $\delta^{15}N$ profile produced by the model with barometric pumping and a time step of 3.5 days (default setting) relative to results obtained with 5x higher temporal resolution (assumed to yield the "true" solution). The error is quantified in the depth range of 68-75 m at WAIS Divide and converges at less than 0.5 per meg after ~30 years. The pressure forcing was linearly interpolated for the high-resolution run and the model was initialized with the steady-state solution presented in the main text for both time steps.

1.2   Layering

We solve the trace gas transport equation under the consideration of discontinuous, impermeable, horizontal layers. Owing to computational limitations, layers cannot be resolved directly in the model and are thus idealized by assigning them an infinitesimal thickness. The discretization of Eq. (S1) using a staggered grid as in Eqs. (S3) and (S4) greatly simplifies the implementation of these impermeable layers.

Layers are advected with the firn. The z-axis position of layer l, at time t, is found by numerically integrating the equation

$$z_l(t) = z_l(t_0) + \int_{t_0}^{t} w_{firn}(z_l(t')) \, dt' , \tag{S6}$$

where z_l is the depth of the layer and w_{firn} is the vertical firn advection velocity. Equation (S6) is discretized using Forward Euler time stepping such that

$$z_l(t) = z_l(t - \Delta t) + w_{firn}\big(z_l(z - \Delta t)\big)\Delta t . \tag{S7}$$

Layer positions on the discrete grid are updated once a layer has moved below the depth of the next grid box. New layers are introduced at 70% of the total depth of the firn column (i.e. $z(\tilde{s} > 0)$) once the top layer was displaced by at least the thickness of one annual layer from its initial position. The centre of each layer opening alternates between two locations (separated by half the horizontal domain length) and the layer size increases linearly with depth. Layers begin to cover the entire horizontal range of the model when the COD is reached and are not tracked further below this depth because any further gas transport is limited to advection with the pores.

1.3   Boundary conditions

A set of boundary and initial conditions accompany Eq. (S1):

1) The model is initialized with isotopic ratios as expected from gravitational equilibrium at all depth. For CO_2 and CH_4 transport simulations, initial concentrations are set to the lowest atmospheric concentrations observed for the time window of the simulation.

2) Surface values of q are given by the atmospheric trace gas concentration at each time step (i.e., a Dirichlet boundary). Atmospheric isotope ratios are assumed to be constant. Atmospheric CO_2 and CH_4 histories are taken and updated from Buizert et al. (2012) based on a combination of direct measurements and reconstructions from the Law Dome ice core site (Figure S4) (Dlugokencky et al., 2016a, 2016b, Etheridge et al., 1996, 1998; Keeling et al., 2001).

3) A periodic boundary condition is implemented for all horizontal fluxes by connecting both sides of the domain.

4) Because Eq. (S1) only describes the trace gas evolution in open pore space, the bottom of the domain is reached where $\tilde{s}$ equals zero. A Neumann boundary condition is chosen for this boundary and the flux leaving through the bottom of the domain is equal to the advection of pores with the firn. Diffusion already ceases to occur at the considerably shallower close-off depth (COD). Because the advective flux at the bottom boundary depends on q, it must be approximated locally using a backward difference scheme.

5) Layers are implemented on the staggered grid by setting the diffusivity and permeability between two adjacent boxes to zero. Layers have an infinitesimally small thickness and do not change the porosity anywhere. The permeability increases from layer edges towards the centre of the layer opening as if porosity in the layer opening increased linearly to obtain a more realistic flow field near layer edges. Other firn properties, such as the diffusivity, are only changed on layers grid points because their porosity-dependence should be considerably weaker than for permeability. Vertical gas advection velocities on layers correspond to the local velocity of firn such that mixing ratio discontinuities are preserved and correctly advected downward at the same speed as layers. Layers do not directly impact the horizontal diffusion, permeability or porosity.
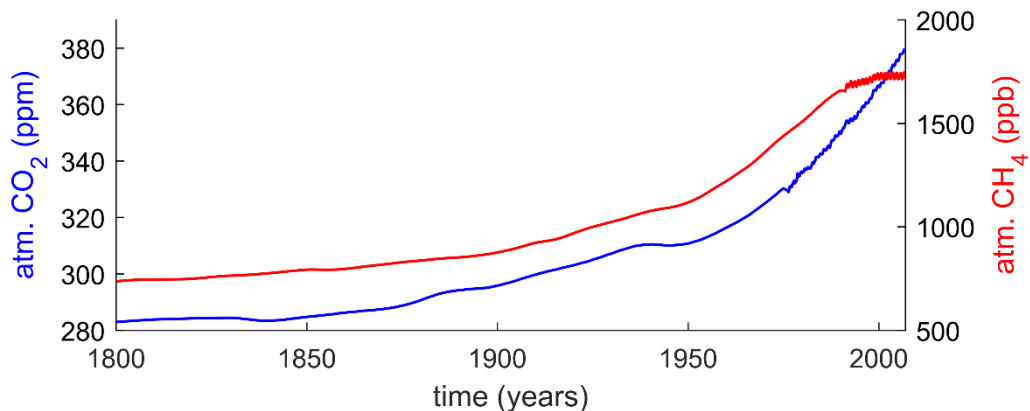
Figure S4. Atmospheric CO_2 and CH_4 histories composed from a combination of direct measurements and reconstructions from the Law Dome ice core site (Buizert et al., 2012; Dlugokencky et al., 2016a, 2016b, Etheridge et al., 1996, 1998; Keeling et al., 2001).

2   Flow field models for firn advection and barometric pumping

2.1   Firn pore advection and pore compression

Advection in the Eularian frame of the model has three components that combine to form the vector $\vec{u}$ in Eq. (S1). The first component of advection represents the downward migration of firn and air contained in the pore spaces due to the continuous accumulation of fresh snow at the surface. This flux can easily be calculated from the snow/ice mass balance and the density profile of the firn. Secondly, the compression of pores in the firn squeezes air out and drives a macroscopic airflow from the firn back to the atmosphere. Finally, barometric pumping drives direction-reversing airflows in response to surface pressure anomalies. These airflows act to return firn air pressures to hydrostatic balance. Barometric pumping flows are orders of magnitude faster than the other fluxes (Fig. 4c) but cause no net airflow when averaged over seasonal or longer time scales. Nevertheless, the fast flow speeds associated with barometric pumping may produce notable dispersive mixing in the deep firn (Buizert and Severinghaus, 2016).

The return and barometric pumping flows $\vec{u}_r$ and $\vec{u}_b$ move through the porous firn medium and obey Darcy's law. Darcy's law (Darcy, 1856) states that the equilibrium-state volume transport $\vec{Q}$ through the cross-sectional area A for laminar, incompressible flow is given by

$$\vec{Q} = -A\frac{\kappa}{\mu}\nabla P \, , \qquad\qquad\qquad (S8)$$

where κ is permeability of the medium (m^2), μ is dynamic viscosity of the fluid (Pa·s), and ∇P is pressure gradient (Pa m^{-1}) driving the flow. We note that the hydrostatic component of pressure ($\tilde{P}$) is no cause of flow and can thus be removed in the flow field model. Discharge $\vec{Q}$ must be divided by area A and the pressure-corrected open porosity $\tilde{s}$ to obtain the true flow speed $\vec{u}$ per pore-cross sectional area used in the tracer advection equation because only a fraction of the total area is available for flow

$$\vec{u} = \frac{\vec{Q}}{A\,\tilde{s}} = -\frac{\kappa}{\mu\,\tilde{s}}\nabla\tilde{P}' . \qquad\qquad\qquad (S9)$$

The continuity equation for a compressible fluid in a porous medium can be derived from the conservation equation of air molecules, using the ideal gas law, which yields

$$\frac{\partial(s_{op}\,\rho)}{\partial t} + \nabla\cdot(s_{op}\,\rho\,\vec{u}) = s_{op}\,S \, , \qquad\qquad\qquad (S10)$$

where ρ is air density and S denotes a source or sink of mass (Buizert and Severinghaus, 2016). Assuming porosity is independent of time, $\frac{\partial(s_{op})}{\partial t} = 0$, and the density in the firn is obtained from hydrostatic balance of an isothermal atmosphere, $\rho \simeq \rho_0 \exp\left(\frac{g\,M}{R\,T}\,z\right)$, the continuity equation implies that

$$\nabla \cdot (\tilde{s}\,\vec{u}) = \frac{\tilde{s}\,S}{\rho_0} - \frac{\partial(\rho_0)}{\partial t} \equiv \alpha\,, \tag{S11}$$

where ρ_0 is surface air density, α is a volume source or sink of air. The depth dependency of density has been absorbed into the open porosity as before. Equation (S11) shows that the divergence of the porosity-scaled velocity must equal the local source of air and change in density.

For the return flow of air to the atmosphere (i.e., $\vec{u}_r$) the source term α_r is the compression of pores during firn advection and density changes are neglected

$$\alpha_r = \nabla \cdot (\tilde{s}\,\vec{u}_r) = \nabla \cdot \left[-\frac{\kappa}{\mu}\nabla\tilde{P}' \right], \tag{S12}$$

and for barometric pumping component of flow (i.e., $\vec{u}_b$) the source or sink α_b is the local density change in response to surface pressure anomalies

$$\alpha_b = \nabla \cdot (\tilde{s}\,\vec{u}_b) = \nabla \cdot \left[-\frac{\kappa}{\mu}\nabla\tilde{P}' \right]. \tag{S13}$$

α_r can be calculated as the vertical derivative of the mean vertical flow due to pore compression $\langle w_r \rangle = w_{air} - w_{firn}$, where w_{air} is the mean effective vertical air transport velocity (m s^{-1}), such that

$$\alpha_r = \frac{\partial}{\partial z}\left[\tilde{s}\left(w_{air} - w_{firn}\right)\right]. \tag{S14}$$

This is analogous to calculating pore compression in a 1D firn column (Rommelaere et al., 1997). At steady-state, mass conservation of air requires that the net vertical flux of air molecules is equal at all depth when integrated horizontally. Using the ideal gas law, the total vertical transport of air molecules n per area A is given by

$$\frac{n}{A\,t} = \frac{P\frac{V}{t}}{A\,R\,T} = \frac{1}{R\,T}\left(\tilde{P}s_{op}w_{air} + P_b s_{cl}w_{firn}\right) \equiv \text{const.}, \tag{S15}$$

where $\tilde{P}$ is the ambient hydrostatic pressure in open pores, P_b is pressure of air in bubbles, and s_{cl} is closed porosity (m^3 m^{-3}). Temporal changes in $\tilde{P}$ are small and their impact on w_{air} and P_b is neglected in Eq. (S15). At $z = z(\text{COD})$, vertical airflow

ceases and air is only carried further downward by the advection of pores with the firn. Therefore, w_{air} is equal to the advection velocity at and below this depth and

$$\frac{n}{A\,t} = \frac{1}{R\,T}\left(\tilde{P}s_{op}w_{firn} + P_b s_{cl}w_{firn}\right)_{|z=z_{COD}}. \tag{S16}$$

For given bubble pressure P_b, Eqs. (S15) and (S16) can be solved to find w_{air} and α_r at all depths. Rommelaere et al. (1997) derive an equation for the change in bubble air content based on the compression of previously existing bubbles and

5   the trapping of air in new bubbles

$$P_b(z) = \frac{1}{w_{firn}\,s_{cl}}\int_0^z \tilde{P}\,w_{firn}s_t\,\frac{\partial}{\partial z}\left(\frac{s_{cl}}{s_t}\right)\,dz\,, \tag{S17}$$

where $s_t \equiv s_{cl} + s_{op}$ is total porosity. Typical pressure profiles are shown in Fig. S5. High P_b near the surface results from the very small, but non-zero closed porosity values that are an artefact of the porosity parameterization at that depth. Mean P_b in the top $\sim$60 % of the firn column above the COD should thus be interpreted with caution.
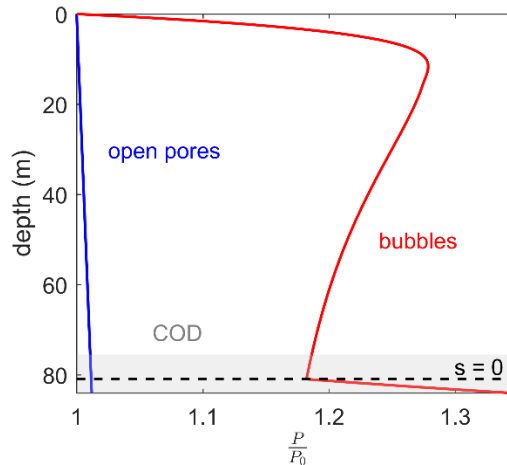
10   **Figure S5.** Normalized profiles of pressure in bubbles and of hydrostatic pressure in open pores at WAIS Divide.

Equations (S12), (S14), (S15), and (S17) are combined to calculate the hypothetical pressure fields for the return flow

$$\frac{\partial}{\partial z}\left[\tilde{s}\left(w_{air} - w_{firn}\right)\right] = \nabla\cdot\left[-\frac{\kappa}{\mu}\nabla\tilde{P}'\right]. \tag{S18}$$

Subsequently, the corresponding velocity field $\vec{u}_r$ is obtained using Eq. (S9). Plots of a representative pressure anomaly field and corresponding flow field are shown in Figs. S6 and S7.
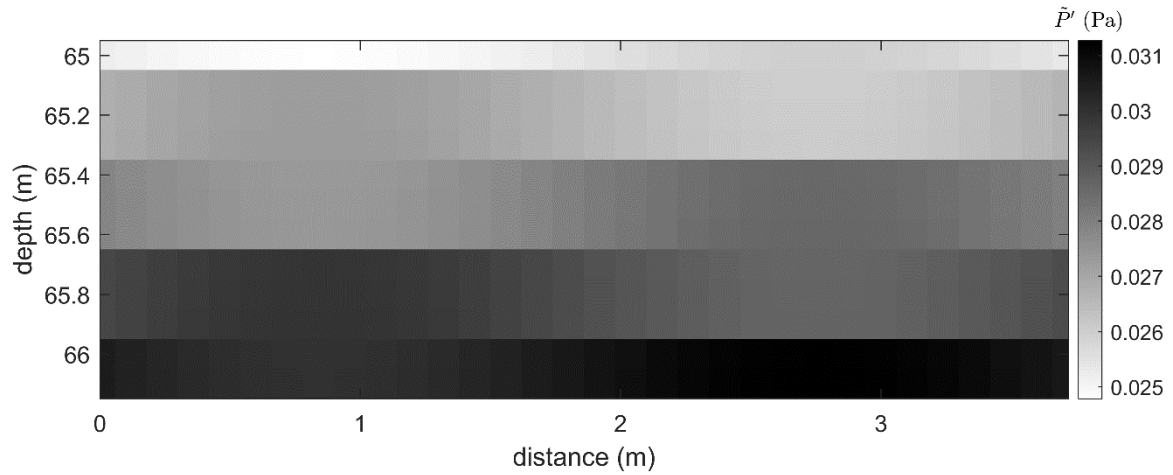
Figure S6. Pressure anomaly field calculated for the return flow to the atmosphere shown in Fig. S7. Layers appear as discontinuities in the pressure field on the model domain. Plot is shown at reduced grid resolution for clarity.
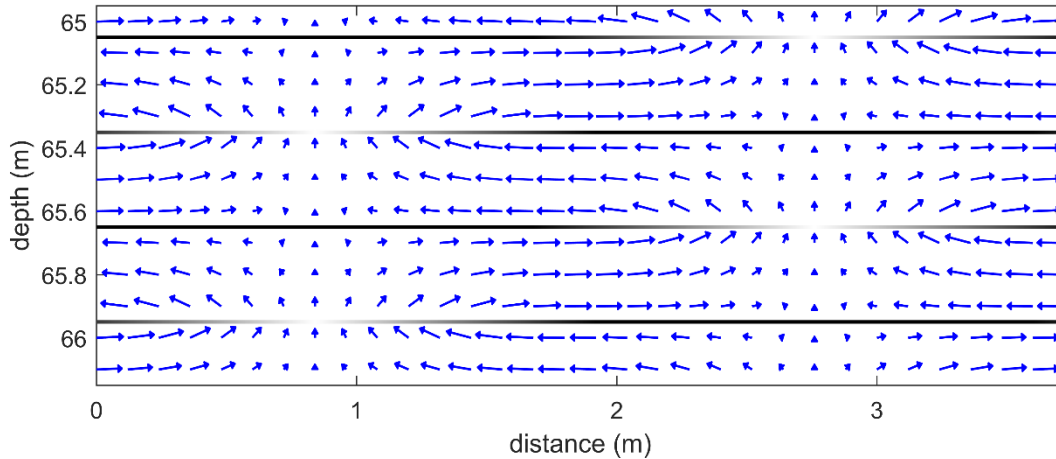
Figure S7. Return flow of air to the atmosphere corresponding to Fig. S6. Plot is shown at reduced grid resolution for clarity.

2.2   Barometric pumping

The source term for barometric pumping, α_b, is equal to the change in firn air density caused by surface pressure anomalies associated with passing storms. Air compression or expansion demands a local convergence or divergence of flow that forces air to move in or out of the firn, assuming porosity remains constant.

Starting from Darcy's law, the continuity equation and hydrostatic balance, Buizert and Severinghaus (2016) derive a partial differential equation for firn air pressure similar to Eq. (S19)

$$s_{op} \frac{\partial P}{\partial t} = \nabla \cdot \left[s_{op} \, \bar{P}_0 \exp\left(\frac{M \, g}{R \, T} z\right) \frac{\kappa}{\tilde{s}\mu} \nabla \tilde{P}' \right]. \tag{S19}$$

Here, we chose not to expand the divergence operator, remove the hydrostatic component of pressure through the definition of $\tilde{P}'$ and use the version of Darcy's law given by Eq. (S9) instead. Following Buizert and Severinghaus (2016), we linearized Eq. (S19) in the pressure anomaly by replacing the pressure (or equivalently the density) in the continuity equation by the annual mean hydrostatic pressure $\left(P = \bar{P}_0 \exp\left(\frac{M \, g}{R \, T} z\right) \right)$. However, the high computational costs of running a 2D model prevent

5   us from reducing the time step below ~3 days and explicitly resolving the propagation of surface pressure waves into firn. Instead, we assume the pressure changes on the LHS should be approximately in hydrostatic balance throughout the firn, in line with results by Buizert and Severinghaus (2016)

$$\frac{\partial P}{\partial t} \simeq \frac{\partial \tilde{P}}{\partial t} = \frac{\partial P_0}{\partial t} \exp\left(\frac{M \, g}{R \, T} z\right), \tag{S20}$$

where $P_0 = P_0(t)$ is the time-varying surface pressure. Combining Eqs. (S19) and (S20) yields α_b

$$\alpha_b \equiv \frac{\tilde{s}}{\bar{P}_0} \frac{\partial P_0}{\partial t}, \tag{S21}$$

and an equation to calculate a hypothetical pressure field which gives rise to the barometric pumping flow

$$\frac{\tilde{s}}{\bar{P}_0} \frac{\partial P_0}{\partial t} = \nabla \cdot \left[\frac{\kappa}{\mu} \nabla \tilde{P}' \right], \tag{S22}$$

10 where $\bar{P}_0$ is the annual mean surface pressure. The flow field, found using Eq. (S9), may be interpreted as the flow required over timestep Δt to return the column to hydrostatic balance with a new surface pressure of P_0. To represent storm activity, we prescribe $P_0(t)$ as pseudo red noise. The surface pressure variability in the model is slightly damped compared to observations in order to account for non-hydrostatic changes. This yields comparable mean vertical velocities as published by Buizert and Severinghaus (2016).

15   Similar to Eq. (S1), the flow field models for the return flow and barometric pumping are discretized using central differences on a staggered grid. Values for κ are calculated using the parametrization of Adolph and Albert (2014) and μ is assumed to be constant. Surface values of $\tilde{P}'$ are set to zero for the return flow and to $P_0(t) - \bar{P}_0$ for barometric pumping. The grid is periodic in the x-direction and no fluxes through the bottom boundary are permitted. Layers set the permeability κ, and thus also velocities, between grid boxes to zero. Because layers are advected with the firn, the total flow field must be

20 recalculated at every time step.

3   Thermal model

We use the thermal model of Alley and Koci (1990) to obtain temperature fields for all time steps. The temperature evolution of firn and ice can be simulated in 1D because horizontal temperature gradients are negligibly small. Heat transport in firn is governed by a slightly modified version of the traditional heat equation (Cuffey, K.M. and Paterson, 2010)

$$\rho c_p \frac{\partial T}{\partial t} = \gamma \frac{\partial^2 T}{\partial z^2} + \frac{\partial \gamma}{\partial z}\frac{\partial T}{\partial z} - \rho c_p w_s \frac{\partial T}{\partial z} + Q \,, \qquad\qquad (S23)$$

5   where T is temperature (°C), $\rho = \rho(z)$ firn density (kg m⁻³), $c_p = c_p(T)$ specific heat capacity of firn (J kg⁻¹ °C⁻¹), $\gamma = \gamma(T, \rho)$ heat conductivity (W m⁻¹ °C⁻¹), w_s vertical advection velocity of firn

/ice (m s^{-1}), and Q is local heat production due to firn compaction and ice deformation (J s^{-1} m^{-2}). Using the chain rule, this expression can be rewritten in terms of the thermal diffusivity $k = \frac{\gamma}{c_p \rho}$ (m^2 s^{-1}) (Johnsen, 1977) as

$$\frac{\partial T}{\partial t} = k \frac{\partial^2 T}{\partial z^2} + \left[\left(\frac{k}{\rho} + \frac{\partial k}{\partial \rho} \right) \frac{\partial \rho}{\partial y} - w_s \right] \frac{\partial T}{\partial z} + \left[\frac{\partial k}{\partial T} + \frac{k}{c_p} \frac{dc_p}{dT} \right] \left(\frac{\partial T}{\partial z} \right)^2 + Q \ . \tag{S24}$$

Following Alley and Koci (1990) and references therein, we use the following parametrizations for w_s, c_p and k

$$w_s = w_{firn} \left(1 - \frac{\sigma}{\rho_{ice} H} \right), \tag{S25}$$

$$c_p = 2096 + 7.7752 T \ , \tag{S26}$$

$$k = \left(1 - 0.00882(T + 30) \right) \left(-1.229 \times 10^{-14} \rho^3 + 2.1312 \times 10^{-11} \rho^2 - 9.4 \times 10^{-9} \rho + 1.779 \times 10^{-6} \right), \tag{S27}$$

where σ is the cumulative load of firnf

5   above (kg m^{-2}) and H the total thickness of the ice sheet. Q parameterized as

$$Q = \sigma \frac{\dot{b} \, \rho_{ice}}{\rho^3} \frac{\partial \rho}{\partial z} \frac{g}{c_p} + \frac{2 \left(\frac{\dot{b}}{H} \right)^{\frac{4}{3}}}{\rho \, c_p \left(4.26 \times 10^{-13} \exp \left(-\frac{7217}{T + 273.15} \right) \right)^{\frac{1}{3}}}, \tag{S28}$$

where $\dot{b}$ is the ice equivalent accumulation rate (m s^{-1}). Equation (S24) is solved by explicit (forward Euler) time stepping because of the non-linearity in T. Spatial derivatives are approximated by central differences. Since the firn air transport model just requires firn temperature for the last ~200 years, only the top 130 m of the ice sheet are simulated in the temperature model for computational efficiency. The temperature gradient at the bottom boundary is fixed to zero but temperature at that depth

10   can evolve freely. Surface temperature histories for WAIS Divide and Law Dome DSS were previously published by Orsi et al. (2012), Van Ommen et al. (1999) and Dahl-Jensen et al. (1999) and allow us to develop a surface forcing for the model. For the Law Dome site DSSW20K, we combine the water oxygen isotope record translated to temperature following Van Ommen et al. (1999) and supplemented this published, six centuries long record with the rescaled mean annual temperature recorded at the nearby Casey Station for the last ~50 years (Jones and Reid, 2001). Further information on the isotope to

15   temperature scaling and the relationship to the historic data at Casey station can be found in Van Ommen et al. (1999). An appropriate offset is applied to the isotope and instrumental temperatures to match the slightly different mean annual temperature at DSSW20K compared to DSS. The Orsi et al. (2012) best fit WAIS Divide surface temperature record is modified slightly to bring our model results in line with the published borehole temperature profiles. A generic Antarctic seasonal cycle is superimposed on both long-term temperature forcings. The seasonal cycle is generated by matching a sine

and cosine wave including serval harmonic to a climatology of Automated Weather Station data at WAIS Divide and Law Dome (Lazzara et al., 2012). The exact details of the seasonal cycle are of limited importance for trace gas transport to the lock-in zone because the seasonal temperature wave becomes quickly attenuated in the firn. We do not mean to imply that our forcings are necessarily accurate reconstructions of local surface temperature but the forcings should yield approximately correct thermal gradients in the firn using our model's temperature module. Moreover, thermal fractionation of isotopes only amounts to a comparatively small influence on most isotopes ratios. Thus, an approximately correct temperature profile is sufficient for our purposes. Temperature fields are only used to account for isotope thermal fractionation and any temperature influence on firn densification is neglected.

4 Model parameter summary

Table S1. Overview of important model parameters

Parameters	WAIS Divide	Law Dome DSSW20K
Depth	85 m	65 m
Width	12 x thickness of an annual layer (i.e., $\sim$2-4 m)	
Horizontal grid spacing	0.03 m	
Vertical grid spacing	0.04 m	
Depth of first layer	70% of total firn column height	
Time	1800–2006 in 3.5-day timesteps	1800–1998.05 in 3.5-day timesteps
Temperature T[1,2]	243.15 K	253.45 K
Ice sheet height H	3500 m	1200 m
Surface Pressure [1,2]	789 hPa	850 hPa
Pressure variability	5 hPa day^{-1}	8 hPa day^{-1}
Ice equiv. advection velocity[1,2]	6.9714×10^{-9} m s^{-1}	5.1706×10^{-9} m s^{-1}
CO_2 and CH_4 atmospheric history	Compilation of Law Dome ice core data[3] & direct measurements at South Pole[4] and Mauna Loa[5] corrected for the interhemispheric gradient	
Density of ice[6]	$\rho_{ice} = 916.5 - 0.14438\,(T - 273.15) - 1.517 \cdot 10^{-4}(T - 273.15)^2$ kg m^{-3}	
Free air relative diffusivities to CO_2	Buizert et al. (2012) and references therein	
Convective zone eddy diffusion $D_e = D_{e0}\exp\left(-\dfrac{z}{\tau}\right)$	$D_{e0} = 2.38 \times D_{m0}$ $\tau = 2.5$ m range: $0 - 8$ m + 2 m linear taper	$D_{e0} = 2.4 \times D_{m0}$ $\tau = 3.5$ m range: $0 - 14$ m + 2 m linear taper
Dispersivity[7] (assumed isotropic)	$\alpha(s_{op}) = 1.26 \cdot \exp(-25.7 s_{op})$	
Total porosity	$s_t = 1 - \dfrac{\rho_{firn}}{\rho_{ice}}$	
Closed porosity[8]	$s_{cl} = 0.37 \cdot s_t \left(\dfrac{s_t}{1-\frac{831.2}{\rho_{ice}}}\right)^{-7.6}$	
Firn density fit $<z_{crit1}$	$\rho_{firn} = a_0 + a_1 z + a_2 \cdot \exp[a_3 \cdot (z_{crit1} - z)]$ kg m^{-3}	
$z_{crit1} - z_{crit2}$	$\rho_{firn} = b_0 + b_1 z + b_2 z^2$ kg m^{-3}	
$>z_{crit2}$	$\rho_{firn} = \rho_{ice} - \left(\rho_{ice} - \rho(z_{crit2})\right) \cdot \exp\left[-\dfrac{z - z_{crit2}}{\rho_{ice} - \rho(z_{crit2})}(b_1 + 2 \cdot b_2 z_{crit2})\right]$ kg m^{-3}	
Density fit parameters[9]	$z_{crit1} = 16$ $z_{crit2} = 110$ $a_0 = 420$ $a_1 = 20.0121$ $a_2 = -151.242$	$z_{crit1} = 19.7186$ $z_{crit2} = 37.4193$ $a_0 = 511.8111$ $a_1 = 7.8210$ $a_2 = -0.0476$

$$a_3 = -0.1$$
$$b_0 = 506.85$$
$$b_1 = 5.3748$$
$$b_2 = -0.0152$$

$$a_3 = 0.4143$$
$$b_0 = 556.5176$$
$$b_1 = 5.3204$$
$$b_2 = 0.0117$$

[1] WAIS Divide: WAIS Divide Project Members (2016)

[2] Law Dome: Etheridge et al. (1992)

[3] Etheridge et al. (1996, 1998) and MacFarling Meure et al. (2006)

[4] Dlugokencky et al. (2016a) and Dlugokencky et al. (2016b)

[5] Keeling et al. (2001) and Dlugokencky et al. (2016b)

[6] Eq: Schwander et al. (1997)

[7] original Eq: Buizert and Severinghaus (2016)

[8] Eq: Goujon et al. (2003) in Severinghaus et al. (2010) and Kawamura et al. (2013)

[9] data: Trudinger et al. (1997); WAIS Divide coefficients: Battle et al. (2011)

5   Law Dome DSSW20K firn properties
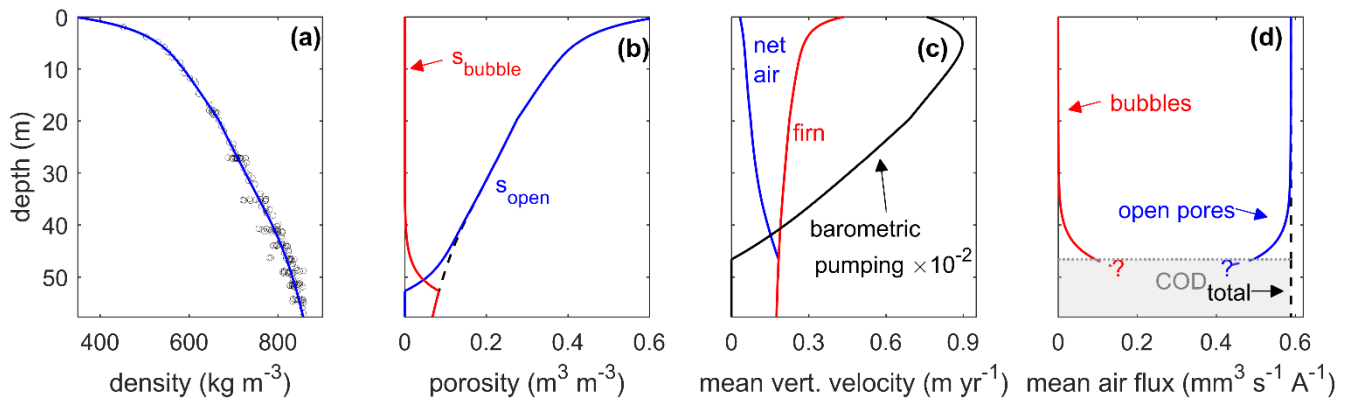
Figure S8. Same as Fig. 4 for Law Dome DSSW20K. Density data: Trudinger et al. (2002, 2013)
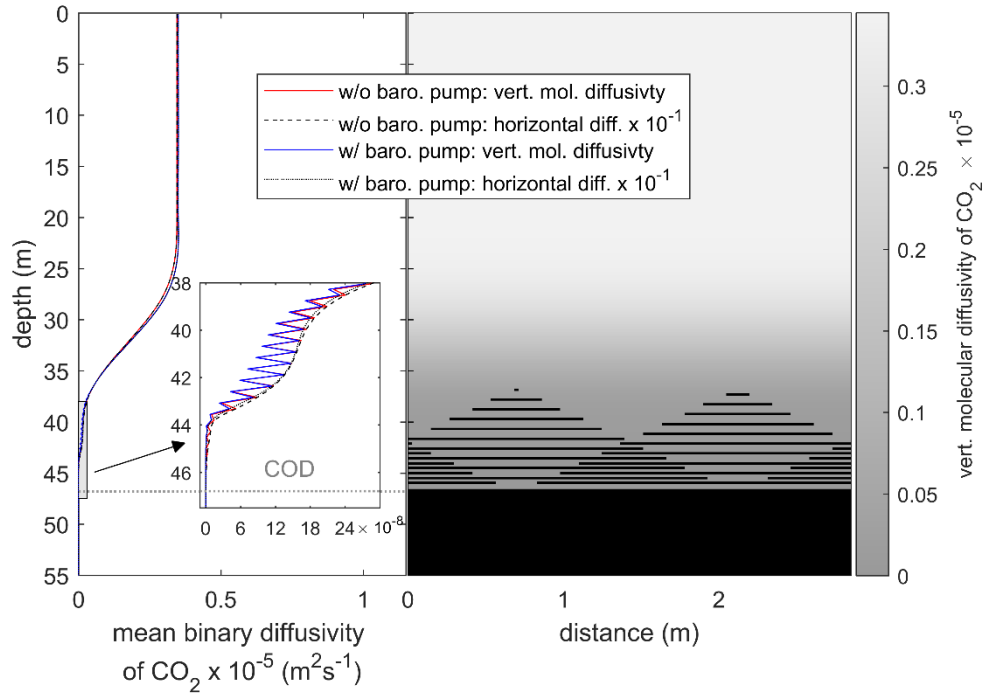
Figure S9. Same as Fig. 6 for Law Dome DSSW20K. Every third annual layer is shown.

6   Mass normalization

Isotope ratios in delta notation are mass-normalized when mentioned to an isotope mass difference of one atomic mass unit

5   (amu) using q-values

$$q_{norm} = q^{\frac{1}{1000 \times \Delta m}}.$$ (S29)

This is more accurate than dividing the ratio in delta notation by the isotope mass difference in amu (e.g. divide $\delta^{40}Ar/^{36}Ar$ by ~4 amu).

7   WAIS Divide CO₂ profile comparison

Four different versions of the 2D model are presented for WAIS Divide in the text. They represent combinations of active and

10   inactive barometric pumping and the presence or absence of layers in the model. 2D models without layers contain no horizontal inhomogeneities and are thus reduced to 1D for computational efficiency but contain essentially the same physics and numerical implementation. Diffusivities in both 1D models are automatically tuned such that the CO_2 profiles are (nearly) identical to the corresponding 2D versions. The use of an automatic tuning procedure to match the CO_2 and CH_4 profiles of

any 2D version of the model is prohibited by the high computational costs of running a 2D model. Differences in the CO_2 profiles between the different models are shown in Fig. S10.
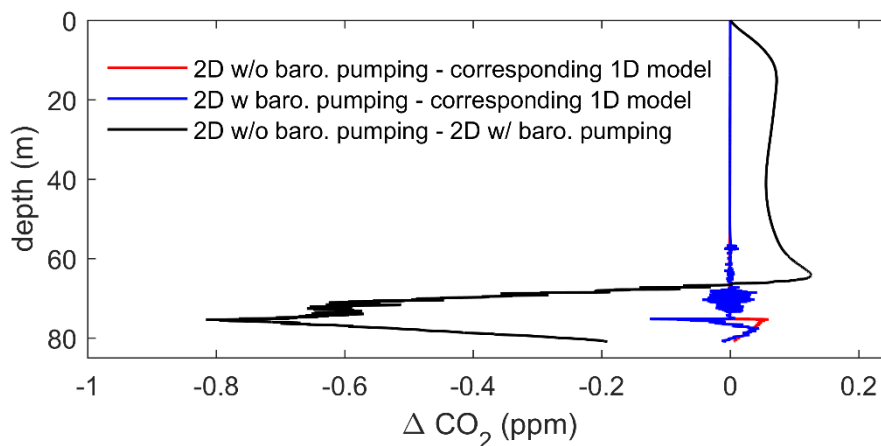
Figure S10. Comparison of simulated CO_2 values at WAIS Divide between both 2D models (black line) and between each 2D model and the corresponding 1D model (red and blue line).

8   Predicting kinetic isotope fractionation at WAIS Divide

Kinetic isotope fractionation (ϵ') of the krypton-nitrogen ratio can be directly related to ϵ' of krypton isotopes. A linear fit yields the relationship shown in Fig. S11 and discussed in the text.
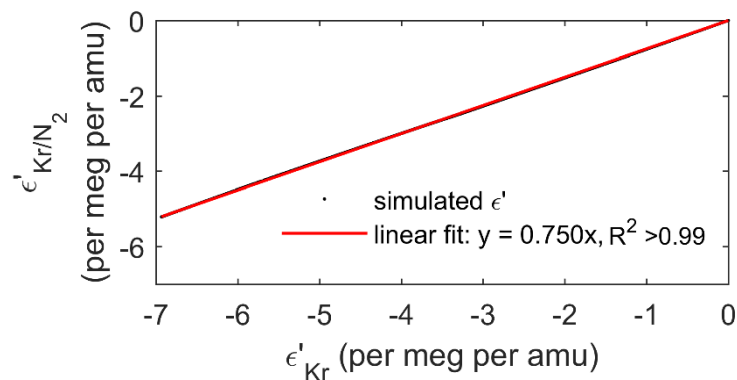
Figure S11. Linear fit to the relationship between mass-normalized ϵ' of $^{84}Kr/^{28}N_2$ and ϵ' of $^{86}Kr/^{82}Kr$ observed in the 2D model with barometric pumping at WAIS Divide.

9   References

Adolph, A. C. and Albert, M. R.: Gas diffusivity and permeability through the firn column at Summit, Greenland: Measurements and comparison to microstructural properties, Cryosphere, 8(1), 319–328, doi:10.5194/tc-8-319-2014, 2014.

Alley, R. B. and Koci, B. R.: Recent warming in central Greenland?, Annals of Glaciology, 14, 6–8, 1990.

Battle, M. O., Severinghaus, J. P., Sofen, E. D., Plotkin, D., Orsi, A. J., Aydin, M., Montzka, S. A., Sowers, T. and Tans, P. P.: Controls on the movement and composition of firn air at the West Antarctic Ice Sheet Divide, Atmospheric Chemistry and Physics, 11, 11007–11021, doi:10.5194/acp-11-11007-2011, 2011.

Buizert, C. and Severinghaus, J. P.: Dispersion in deep polar firn driven by synoptic-scale surface pressure variability, The Cryosphere Discussions, 2016, 1–21, doi:10.5194/tc-2016-148, 2016.

Buizert, C., Martinerie, P., Petrenko, V. V, Severinghaus, J. P., Trudinger, C. M., Witrant, E., Rosen, J. L., Orsi, A. J., Rubino, M., Etheridge, D. M., Steele, L. P., Hogan, C., Laube, J. C., Sturges, W. T., Levchenko, V. A., Smith, A. M., Levin, I., Conway, T. J., Dlugokencky, E. J., Lang, P. M., Kawamura, K., Jenk, T. M., White, J. W. C., Sowers, T., Schwander, J. and Blunier, T.: Gas transport in firn: Multiple-tracer characterisation and model intercomparison for NEEM, Northern Greenland, Atmospheric Chemistry and Physics, 12, 4259–4277, doi:10.5194/acp-12-4259-2012, 2012.

Cuffey, K.M. and Paterson, W. S. .: The Physics of Glaciers, 4th ed., Butterworth-Heinemann/Elsevier, Burlington, MA., 2010.

Dahl-Jensen, D., Morgan, V. I. and Elcheikh, A.: Monte Carlo inverse modelling of the Law Dome (Antarctica) temperature profile, Annals of Glaciology, 29, 145–150, doi:10.3189/172756499781821102, 1999.

Darcy, H.: Les Fontaines Publiques de la Ville de Dijon, Victor Dalmont, Paris., 1856.

Dlugokencky, E. J., Lang, P. M., Mund, J. W., Crotwell, A. M., Crotwell, M. J. and Thoning, K. W.: Atmospheric Carbon Dioxide Dry Air Mole Fractions from the NOAA ESRL Carbon Cycle Cooperative Global Air Sampling Network, 1968-2015, Version: 2016-08-30, 2016a.

Dlugokencky, E. J., Lang, P. M., Crotwell, A. M., Mund, J. W., Crotwell, M. J. and Thoning, K. W.: Atmospheric Methane Dry Air Mole Fractions from the NOAA ESRL Carbon Cycle Cooperative Global Air Sampling Network, 1983-2015, Version: 2016-07-07, 2016b.

Etheridge, D. M., Pearman, G. I. and Fraser, P. J.: Changes in tropospheric methane between 1841 and 1978 from a high accumulation-rate Antarctic ice core, Tellus, 44B, 282–294, doi:10.1034/j.1600-0889.1992.t01-3-00006.x, 1992.

Etheridge, D. M., Steele, L. P., Langenfelds, R. L., Francey, R. J., Barnola, J. M. and Morgan, V. I.: Natural and anthropogenic changes in atmospheric CO_2 over the last 1000 years from air in Antarctic ice and firn, Journal of Geophysical Research-Atmospheres, 101(D2), 4115–4128, doi:10.1029/95JD03410, 1996.

Etheridge, D. M., Steele, L. P., Francey, R. J. and Langenfelds, R. L.: Atmospheric methane between 1000 A.D. and present: Evidence of anthropogenic emissions and climatic variability, Journal of Geophysical Research, 103(D13), 15979, doi:10.1029/98JD00923, 1998.

Goujon, C., Barnola, J.-M. and Ritz, C.: Modeling the densification of polar firn including heat diffusion: Application to close-off characteristics and gas isotopic fractionation for Antarctica and Greenland sites, Journal of Geophysical Research, 108, 4792, doi:10.1029/2002JD003319, 2003.

Johnsen, S. J.: Stable isotope profiles compared with temperature profiles in firn with historical temperature records,

Isotopes and Impurities in Snow and Ice, 388–392, 1977.

Jones, P. D. and Reid, P. A.: A databank of Antarctic surface temperature and pressure data, ORNL/CDIAC-27, NDP-032, Carbon Dioxide Information Analysis Center, Oak Ridge National Laboratory, U.S. Department of Energy, Oak Ridge, Tennessee., 2001.

5   Kawamura, K., Severinghaus, J. P., Albert, M. R., Courville, Z. R., Fahnestock, M. A., Scambos, T. A., Shields, E. and Shuman, C. A.: Kinetic fractionation of gases by deep air convection in polar firn, Atmospheric Chemistry and Physics, 13, 11141–11155, doi:10.5194/acp-13-11141-2013, 2013.

Keeling, C. D., Stephen, C., Piper, S. C., Bacastow, R. B., Wahlen, M., Whorf, T. P., Heimann, M. and Meijer, H. A.: Exchanges of atmospheric CO2 and 13CO2 with the terrestrial biosphere and oceans from 1978 to 2000., Global Aspects, SIO 10   Reference Series. Scripps Institution of Oceangraphy, San Diego, 01–06, 83–113, doi:10.1007/b138533, 2001.

Lazzara, M. A., Weidner, G. A., Keller, L. M., Thom, J. E. and Cassano, J. J.: Antarctic automatic weather station program: 30 years of polar observations, Bulletin of the American Meteorological Society, 93, 1519–1537, doi:10.1175/BAMS-D-11-00015.1, 2012.

MacFarling Meure, C., Etheridge, D., Trudinger, C., Steele, P., Langenfelds, R., Van Ommen, T., Smith, A. and Elkins, J.: 15   Law Dome CO2, CH4 and N2O ice core records extended to 2000 years BP, Geophysical Research Letters, 33(L14810), 1–4, doi:10.1029/2006GL026152, 2006.

Van Ommen, T. D., Morgan, V. I., Jacka, T. H., Woon, S. and Elcheikh, A.: Near-surface temperatures in the Dome Summit South (Law Dome, East Antarctica) borehole, Annals of Glaciology, 29, 141–144, doi:doi:10.3189/172756499781821382, 1999.

20   Orsi, A. J., Cornuelle, B. D. and Severinghaus, J. P.: Little Ice Age cold interval in West Antarctica: Evidence from borehole temperature at the West Antarctic Ice Sheet (WAIS) Divide, Geophysical Research Letters, 39(L09710), 1–7, doi:10.1029/2012GL051260, 2012.

Rommelaere, V., Arnaud, L. and Barnola, J.-M.: Reconstructing recent atmospheric trace gas concentrations from polar firn and bubbly ice data by inverse methods, Journal of Geophysical Research, 102(D25), 30069–30083, 1997.

25   Schwander, J., Sowers, T., Barnola, J. M., Blunier, T., Fuchs, A. and Malaizé, B.: Age scale of the air in the summit ice: Implication for glacial-interglacial temperature change, Journal of Geophysical Research, 102(D16), 19483–19493, doi:10.1029/97JD01309, 1997.

Severinghaus, J. P., Albert, M. R., Courville, Z. R., Fahnestock, M. A., Kawamura, K., Montzka, S. A., Mühle, J., Scambos, T. A., Shields, E., Shuman, C. A., Suwa, M., Tans, P. and Weiss, R. F.: Deep air convection in the firn at a zero-accumulation 30   site, central Antarctica, Earth and Planetary Science Letters, 293, 359–367, doi:10.1016/j.epsl.2010.03.003, 2010.

Trudinger, C. M., Enting, I. G., Etheridge, D. M., Francey, R. J. and Steele, L. P.: Modeling air movement and bubble trapping in firn, Journal of Geophysical Research, 102, 6747–6763, doi:10.1029/96JD03382, 1997.

Trudinger, C. M., Etheridge, D. M., Rayner, P. J., Enting, I. G., Sturrock, G. A. and Langenfelds, R. L.: Reconstructing atmospheric histories from measurements of air composition in firn, Journal of Geophysical Research Atmospheres, 107(24),

1–13, doi:10.1029/2002JD002545, 2002.

Trudinger, C. M., Enting, I. G., Rayner, P. J., Etheridge, D. M., Buizert, C., Rubino, M., Krummel, P. B. and Blunier, T.: How well do different tracers constrain the firn diffusivity profile?, Atmospheric Chemistry and Physics, 13, 1485–1510, doi:10.5194/acp-13-1485-2013, 2013.

5   WAIS Divide Project Members: WAIS Divide Site Characteristics, [online] Available from: http://www.waisdivide.unh.edu (Accessed 15 November 2016), 2016.